

Acceleration of Compact Radio Jets on Sub-parsec Scales

Sang-Sung Lee^{1,2}, Andrei P. Lobanov³, Thomas P. Krichbaum³, and J. Anton Zensus³

ABSTRACT

Jets of compact radio sources are highly relativistic and Doppler boosted, making studies of their intrinsic properties difficult. Observed brightness temperatures can be used to study the intrinsic physical properties of the relativistic jets, and constrain models of jet formation in the inner jet region. We aim to observationally test such inner jet models. The very long baseline interferometry (VLBI) cores of compact radio sources are optically thick at a given frequency. The distance of the core from the central engine is inversely proportional to the frequency. Under the equipartition condition between the magnetic field energy and particle energy densities, the absolute distance of the VLBI core can be predicted. We compiled the brightness temperatures of VLBI cores at various radio frequencies of 2, 8, 15, and 86 GHz. We derive the brightness temperature on sub-parsec scales in the rest frame of the compact radio sources. We find that the brightness temperature increases with increasing distance from the central engine, indicating that the intrinsic jet speed (the Lorentz-factor) increases along the jet. This implies that the jets are accelerated in the (sub-)parsec regions from the central engine.

Subject headings: galaxies: active — galaxies: jets — galaxies: nuclei — radio continuum: galaxies — quasars: general

1. Introduction

Relativistic jets are frequently observed in many compact astronomical objects such as gamma-ray bursts (GRB) (Kulkarni et al. 1999; Greiner et al. 2003), X-ray binaries (XRB or microquasars) (Mirabel & Rodriguez 1994, 1998), and active galactic nuclei (AGN) (Curtis 1918; Baade & Minkowski 1954; Bridle & Perley 1984). Deep insights into the processes governing the generation, the physics, and the behavior of the relativistic jets can be obtained by studying the differences or consistencies in the properties of these objects. In an effort to understand these processes, the relativistic jets in AGN have been extensively studied (see Kellermann & Pauliny-Toth

1981; Bridle & Perley 1984; Zensus 1997; Ferrari 1998; Harris & Krawczynski 2006).

The apparent velocities of the relativistic jets in powerful AGN show apparent superluminal motions (Rees 1966; Whitney et al. 1971) as high as $\sim 50 c$ (e.g., Lister et al. 2009) in the radio regime, and rapid variability in the flux and polarization of the relativistic jet component on scales ≤ 1 pc. Although the jets may also contain non-relativistic jet components, there is evidence that the relativistic component dominates and extends up to Mpc (e.g., Walker et al. 2001). While the matter content of the relativistic jet remains uncertain, there are indications that protons dominate the mass flux even as electron-positron pairs dominate the particle flux in relativistic AGN jets (Sikora & Madejski 2000). Magnetic fields are considered the most likely driving mechanism on these scales as well (Lovelace 1976; Blandford & Znajek 1977; Blandford & Payne 1982).

In any case, the acceleration mechanism is not well understood in jets, with magnetohydrody-

¹Korea Astronomy and Space Science Institute, 776 Daedeok-daero, Yuseong-gu, Daejeon 34055, Republic of Korea; sslee@kasi.re.kr

²Korea University of Science and Technology, 217 Gajeong-ro, Yuseong-gu, Daejeon 34113, Republic of Korea

³Max-Planck-Institut für Radioastronomie, Auf dem Hügel 69, 53121 Bonn, Germany; alobanov, tkrichbaum, azensus@mpifr-bonn.mpg.de

dynamic (MHD) models (e.g., Vlahakis & Königl 2004; Lyubarsky 2009) currently being one of the favored scenarios. MHD models are contested by models which attribute the mechanism to acceleration by magnetic fields (e.g., Heinz & Begelman 2000; Lovelace & Romanova 2003; McKinney & Blandford 2009; Toma & Takahara 2014; Nokhrina et al. 2015). In particular, McKinney & Blandford (2009) demonstrated jet formation, based on the three-dimensional, general relativistic MHD simulations of rapidly rotating Kerr black holes, and showed that jets may be able to reach up to a Lorentz factor of 10 depending on the field geometry.

The intrinsic properties of extragalactic jets are difficult to measure, owing to the relativistic motion of the jet plasma, which can result in substantial time delays and Doppler boosting in the observer’s frame. Time delays strongly affect optically thin emission along a given path through the jet, and Doppler boosting couples the true physical properties of the emitting material to the geometrical and kinematic conditions in the flow. We would like to derive the evolution of some intrinsic parameters of the flow which can be used as a probe of the acceleration. Brightness temperature measurements of VLBI cores as derived from Very Long Baseline Interferometry (VLBI) are such a probe. It brings us the closest to the central engine, reduces the effect of time delays (important for the optically thin part of the flow), and also reduces the chance of contaminating our measurements due to variable Doppler boosting in a (likely) curved flow downstream of the core.

Observations at 86 GHz are particularly well-suited for this work, since they penetrate closer to the origin of the flow, owing to reduced opacity at higher frequencies. Sensitive VLBI observations at 86 GHz with large radio telescopes, e.g., the Global Millimeter VLBI Array (GMVA, Martí-Vidal et al. 2012), have been made for a few prominent AGN jets, such as 3C 111 (Doeleman & Claussen 1997), 3C 454.3 (Krichbaum et al. 1995, 1999; Pagels et al. 2004), NRAO 150 (Agudo et al. 2007; Molina et al. 2014), NRAO 530 (Bower et al. 1997), M87 (Krichbaum et al. 2006; Hada et al. 2016), Mrk 501 (Giroletti et al. 2008; Koyama et al. 2016), 3C 273, 3C 279 (Attridge 2001; Lee et al. 2015), and S5 0716+714 (Rani et al. 2015). In order to further increase the number of

objects, which can be imaged at 86 GHz, five detection and imaging surveys were conducted during the last few decades, with a total of 167 extragalactic radio sources observed (see Beasley et al. 1997; Lonsdale et al. 1998; Rantakyrö et al. 1998; Lobanov et al. 2000; Lee et al. 2008). In these surveys fringes were detected in 130 objects, and 144 radio sources have been successfully imaged.

In order to derive the intrinsic parameters of the relativistic jets, it is possible to compare the brightness temperatures measured at 86 GHz with those at lower frequencies (e.g., 2 – 15 GHz). As shown in Lee (2013), the brightness temperatures of the VLBI cores imaged at 86 GHz are found to be lower than those at 15 GHz, assuming the brightness temperature on average is the same for all sources, and the viewing angles of the target jets are close to the critical value for the maximal apparent jet speed, following Homan et al. (2006). Careful comparison of the brightness temperatures at multifrequencies, that is, at 2, 8, 15, and 86 GHz enabled the study of the variation of the brightness temperatures as a function of frequency. This suggests that the VLBI cores mark the position of the transition zone between magnetic and kinetic dominance (Lee 2014).

Under the equipartition condition between jet particle and magnetic field energy densities, the position shift of the VLBI cores between two frequencies can be predicted (Lobanov 1998). The brightness temperatures in the rest frame of sources and the predicted core shift can be used to test the inner jet models, by deriving the intrinsic parameters of the relativistic jets.

In this paper, we investigate the evolution of the brightness temperatures (and hence the Lorentz factor) of the relativistic jets by using the frequency dependence of the VLBI core position. In Section 2, we describe a general strategy for compiling the brightness temperatures and a model which was adopted to predict the physical distance of the observed VLBI core from the central engine. In Section 3, we present the evolution of the brightness temperature resulting from the application of the predicted absolute distance of VLBI cores to brightness temperatures in the source frame on (sub-)parsec scales. In Section 4, the intrinsic parameters of the relativistic jets are discussed, and in Section 5 we provide conclusions. Throughout the paper, we use a Hubble constant

$H_0 = 71 \text{ km s}^{-1} \text{ Mpc}^{-1}$ and a cosmological density parameter $\Omega_m = 0.27$.

2. Brightness temperature in ultracompact jets

2.1. General strategy

In order to investigate the physics of compact jets in sub-parsec scale regions, we combined core brightness temperature measurements from 86 GHz (Lee et al. 2008) with measurements obtained at lower frequencies, namely at 2 GHz and 8 GHz (Pushkarev & Kovalev 2012), and 15 GHz (Kovalev et al. 2005). Lee et al. (2008) observed 127 compact radio jets using the GMVA at 86.2 GHz in the period between 2001 October and 2002 October, and imaged 109 jets with a typical resolution of approximately $40 \mu\text{as}$ (i.e. a scale of $< 0.1 \text{ pc}$ at $z = 1$). A 2-dimensional circular Gaussian model was fitted to the VLBI core of each jet for estimating a source-frame core brightness temperature T_b following

$$T_b = 1.22 \times 10^{12} \frac{S}{d^2 \nu^2} (1+z) \text{ K}, \quad (1)$$

where S is the fitted core flux density in Janskys, d is the angular size (or FWHM) of the fitted component in milliarcseconds, and ν is the observing frequency. The factor $(1+z)$ reflects the cosmological effect on the brightness temperature. A core component was considered to be unresolved when its fitted FWHM was smaller than its minimum resolvable size, and hence the brightness temperature was determined to be a lower limit. The minimum resolvable size of a component in a general VLBI image is given by Lobanov (2005) as

$$d_{\min} = 2^{1+\beta/2} \left[\frac{ab \ln 2}{\pi} \ln \left(\frac{SNR}{SNR-1} \right) \right]^{1/2}, \quad (2)$$

where a and b are the axes of the restoring beam of observations, SNR is the signal-to-noise ratio of the jet component, and β is a weighting function of imaging, which is 0 for natural weighting or 2 for uniform weighting. If $d < d_{\min}$ for a core component, then the component is considered to be unresolved and the lower limit of T_b is obtained with $d = d_{\min}$.

Pushkarev & Kovalev (2012) observed a sample of 370 compact radio jets with up to 24 radio telescopes at 2.3 GHz and 8.6 GHz in the

period between 1998 October and 2003 September. The VLBI cores fitted with the circular Gaussian model had median sizes of 1.04 mas ($\sim 6.75 \text{ pc}$) and 0.28 mas ($\sim 1.90 \text{ pc}$) at 2.3 GHz and 8.6 GHz, respectively, and typical core brightness temperatures of $2.5 \times 10^{11} \text{ K}$ at both frequencies. Kovalev et al. (2005) observed 250 compact radio jets with the very long baseline array (VLBA) at 15.4 GHz in the period between 1993 and 2003, with the smallest jet angular size of 0.02-0.06 mas, which corresponds to a linear scale of $< 0.1 \text{ pc}$ for the nearest target. The VLBI cores were fitted with the elliptical Gaussian model, yielding brightness temperatures between $10^{11} - 10^{13} \text{ K}$.

In selecting the core brightness temperatures of the compact radio jets observed at multifrequencies in multiple epochs, the measurements for the lower limits have been excluded. From the multiple epoch measurements of the brightness temperatures at 15 GHz, we have taken their median value in order to take the near equipartition value (Homan et al. 2006). From the compilation of our brightness temperature data base we included a source only when it was observed at more than two frequencies. We found that a total of 109 out of 325 compact radio jets were suitable for the sample as listed in Table 2.

2.2. Ultracompact jet and core shift

Before we present our results, we want to describe the theoretical background. We follow the standard relativistic jet model of Blandford & Königl (1979), who consider an idealized model of a steady radio jet, in order to parametrize a relativistic jet. They assumed a narrow conical jet of small opening angle ϕ whose axis makes an angle θ with the line of sight of the observer (the observed opening angle is $\phi_o = \phi \csc \theta$). The jet is assumed to be supersonic and free, and to have a constant speed β_j . The magnetic field in the jet B should vary as r^{-1} , where r is the distance from the apex of the jet (harboring most likely the central engine). The flow of relativistic particles in the jet is accelerated by converting the internal relativistic particle energy γ_e to the bulk kinetic energy γ_k . Their particle energy distribution is $N(\gamma_e) = N_0 \gamma_e^{-s}$ for $\gamma_{\min}(r) < \gamma_e < \gamma_{\max}(r)$, where s is the particle energy power index. Those electrons radiate inhomogeneous synchrotron radiation with a spectral index $\alpha = (1-s)/2$. For a typ-

ical $\alpha = -0.5$ ($S_\nu \propto \nu^\alpha$), the corresponding particle energy distribution is $N(\gamma_e) = N_0\gamma_e^{-2}$. Assuming the equipartition between the jet particle energy and the magnetic field energy, which is given by $k_e\Lambda B^2/8\pi$ ($k_e \leq 1$ and $\Lambda = \ln(\gamma_{\max}/\gamma_{\min})$), the total radiated synchrotron power from the emission region extending from r_{\min} to r_{\max} in the jet is

$$L_{\text{syn}} = \frac{1}{8}k_e\Delta\gamma_j^2\beta_j cB^2r^2\phi^2, \quad (3)$$

where $\Delta = \ln(r_{\max}/r_{\min})$.

The observed VLBI core at any given frequency is located in the region where the optical depth to synchrotron self-absorption is $\tau_s = 1$. Assuming that the magnetic field and particle density decrease with r as $B = B_1(r_1/r)^m$ and $N = N_1(r_1/r)^n$, where B_1 and N_1 are the magnetic field and the electron density at $r_1 = 1$ pc, respectively, the corresponding τ_s is given by (see Rybicki & Lightman 1979; Lobanov 1998):

$$\tau_s(r) = C_2(\alpha)N_1 \left(\frac{eB_1}{2\pi m_e} \right)^\epsilon \frac{\delta^\epsilon \phi_o}{r^{(\epsilon m + n - 1)\nu^{\epsilon+1}}}, \quad (4)$$

where e , m_e are the electron charge and mass, respectively, and δ , ϕ_o are the Doppler factor and the observed jet opening angle. Here $\epsilon = 3/2 - \alpha$, and $C_2(\alpha)$ is a constant at a given spectral index (Blumenthal & Gould 1970). For a typical spectral index of $\alpha = -0.5$, $C_2(\alpha) = 8.4 \times 10^{10}$ in *cgs* units. The physical distance of the observed VLBI core from the central engine is obtained by setting the optical depth $\tau_s(r)$ to unity:

$$r = [\nu^{-1}(1+z)^{-1}B_1^{k_b}\{6.2 \times 10^{18}C_2(\alpha)\delta_j^\epsilon N_1\phi_o\}^{1/(\epsilon+1)}]^{1/k_r}, \quad (5)$$

where $k_r = \{(3 - 2\alpha)m + 2n - 2\}/(5 - 2\alpha)$ and $k_b = (3 - 2\alpha)/(5 - 2\alpha)$. Königl (1981) showed that it is most reasonable to use $m = 1$ and $n = 2$ to explain the observed X-ray and synchrotron emission from the ultra compact VLBI jets. In this case, the corresponding $k_r = 1$ does not depend on the spectral index. Then, we find a simple evolution of the magnetic field decreasing with r as $B = B_1(r_1/r)$, and hence $Br = B_1r_1 = \text{constant}$. This model can be used to obtain B_1 taking into account Equation (3) as

$$B_1 = \left(L_{\text{syn}} \frac{8}{k_e\Delta} \frac{1}{\gamma_j^2\beta_j c r_1^2 \phi^2} \right)^{1/2}. \quad (6)$$

By inserting Equation (6) into Equation (5), the absolute position of the observed VLBI core r is related with the total radiated synchrotron luminosity L_{syn} as

$$r = \left[\xi C_r L_{\text{syn}}^{k_b/2} \{\nu(1+z)\}^{-1} \right]^{1/k_r} \text{ pc}, \quad (7)$$

with

$$\xi = \left(\frac{8}{k_e\Delta} \right)^{k_b/2} [6.2 \times 10^{18}C_2(\alpha)]^{1/(\epsilon+1)} \quad (8)$$

and

$$C_r = \frac{(\delta_j^\epsilon N_1 \phi_o)^{1/(\epsilon+1)}}{(\gamma_j^2 \beta_j c r_1^2 \phi^2)^{k_b/2}}, \quad (9)$$

where L_{syn} is in erg s⁻¹ and ν is in Hz.

3. Evolution of the brightness temperature

In Figure 1 we combined the brightness temperature measurements obtained at the different frequencies in one plot. We plot the brightness temperature (in the source frame T_b) as a function of frequency in the rest frame of the source, $\nu_0 = \nu(1+z)$. The brightness temperatures observed at 86 GHz are obviously lower than those at lower frequencies (2, 8, and 15 GHz). In Table 1, we quantify this result, where we show for each frequency the median, mean and standard deviation (rms) value of the brightness temperature. From the table it is seen that the median and mean of the 86 GHz brightness temperatures are lower by a factor of 5-6 compared to those of lower frequency brightness temperatures. Despite the uncertainties due to the amplitude calibration error of 20% – 30% at 86 GHz (Lee et al. 2008) and the source variability of a factor of ~ 2 , the brightness temperatures observed at 86 GHz are still relatively lower than those at the lower frequencies, implying that the decrease of brightness temperatures at 86 GHz is significant.

The variation of brightness temperature with frequency can be translated into a variation of brightness temperature as a function of core separation assuming the validity of the relativistic jet model, as in particular using equation (5). With the reasonable assumption of $m = 1$, $n = 2$, we obtain $k_r r = 1$, and therefore $r_{\text{core}} \propto \nu_0^{-1/k_r}$. The decrease of the brightness temperature with frequency (from 400 to 10 GHz in the source frame)

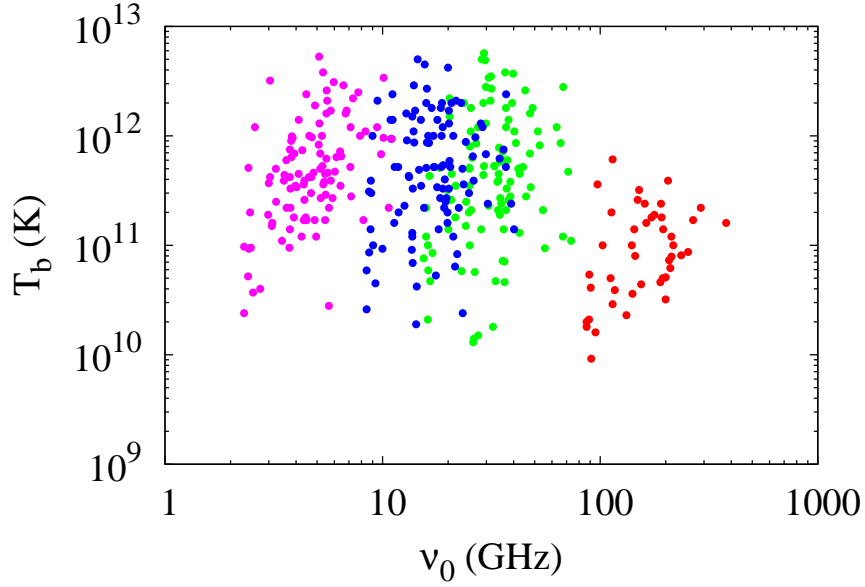


Fig. 1.— Brightness temperatures in the source frame as a function of frequency in the source frame. All available VLBI measurements (excluding lower limits) of core components at 2 GHz (magenta dot), 8 GHz (blue dot), 15 GHz (green dot), and 86 GHz (red dot) for the selected 109 sources.

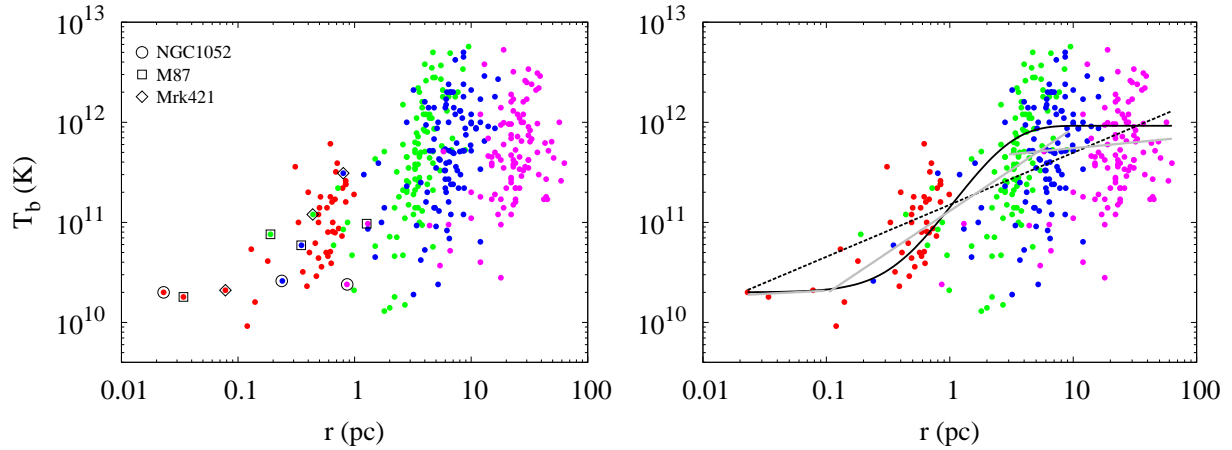


Fig. 2.— [Left] Brightness temperatures in the source frame as a function of the absolute position of the VLBI core components. The used parameters for the deduced position of the VLBI core are $\gamma_j = 10$, $\phi = 1/\gamma_j^2$, $N_1 = 5 \times 10^3 \text{ cm}^{-3}$, and $r_{\text{max}}/r_{\text{min}} = 100$. Colors are the same as for Figure 1. Brightness temperatures for three sources are marked with symbols: circles for 0238–084 (NGC 1052), squares for 1228+126 (M87), and diamonds for 1101+384 (Mrk421). [Right] The same data with the best fits to the data for several cases, as described in Section 4: a single power law fit in black dashed line, multiple power law fits in grey solid line, and a fit of Equation (10) in black solid line.

therefore implies an increase of brightness temperature with core separation by about one order of magnitude.

However, the position of the core not only depends on the source rest frame frequency but also on the synchrotron luminosity of the source (see equation (7)). This may at least partly explain the relatively large scatter of brightness temperature in Figure 1, which indeed is based on many sources with different synchrotron luminosity (see Table 2). Another reason for the scatter may also come from source intrinsic deviations from the idealized power law indices m and n , which may be slightly different for individual sources. Since the particle energy and magnetic field energy densities at 1 pc, B_1 and N_1 , are different from source to source, and usually unknown, one cannot easily determine the absolute position of the core from equation (5) except for the case when the apparent shift of the core position at several frequencies is measured (Lobanov 1998). However, with the assumption of energy equipartition between particle and fields in a relaxed and steady jet, the core position can be predicted with the known synchrotron luminosity L_{syn} using equation (7). The synchrotron luminosity can be estimated from the core flux measurements of each source over the range of rest frame frequencies, $\nu_{0,\text{min}} \leq \nu_0 \leq \nu_{0,\text{max}}$. Fitting the spectrum of the core gives the total flux of the source over the range of frequencies. Then, the synchrotron luminosity L_{syn} can be estimated taking into account the total flux and luminosity distance of each source. In Table 2 we summarize the estimated synchrotron luminosity, which is used together with equation (7) to drive the core separation.

Figure 2 shows the brightness temperatures as a function of the determined core position for all compact jets selected. As described in Section 2.1, all sources are assumed to have the same Lorentz factor $\gamma_j = 10$, jet opening angle $\phi = 1/\gamma_j^2$, and viewing angle $\theta = 1/\gamma_j$. The electron density at 1 pc is $N_1 = 5 \times 10^3 \text{ cm}^{-3}$. The synchrotron emission is assumed to be emitted from the region with the scale factor of $r_{\text{max}}/r_{\text{min}} = 100$ at frequencies of $2 \text{ GHz} \leq \nu_0 \leq 400 \text{ GHz}$. After investigating the change of results depending on γ_j , we found that the distance r of a core observed at a given frequency mildly depends on γ_j , as $r \propto \gamma_j^{0.34}$, yield-

ing, for example, the ranges of $r = 0.023 - 63 \text{ pc}$ for $\gamma_j = 10$ and of $r = 0.050 - 14 \text{ pc}$ for $\gamma_j = 100$. As expected from Figure 1, the brightness temperatures increase from the inner region to the outer region of (sub-)parsec scales, which implies that the energy of the radiating particles increases as they are driven out from the central engine in the (sub-)parsec scale region of the jet.

4. Discussion

4.1. Modeling the radial dependence of brightness temperature

In order to interpret the increase of the brightness temperatures along the jet on the scales of 0.01-100 pc, we modeled it with a single power-law function as shown in Figure 2. One single power-law seems to reasonably fit the data, but in particular on sub-pc scales, a number of data points fall below the best fit line. This may imply that a single power-law fit may not be the best presentation of the radial dependence of brightness temperature. Although the number of data points in each bin of the distance (e.g., 0.01-0.1 pc, 0.1-1 pc, 1-10 pc and 10-100 pc) is different each other, the increasing pattern in the inner region (e.g., 0.01-0.1 pc) looks a bit different from those in the outer region (0.1-10 pc). Moreover the large scatter of data in 1-100 pc may make difficult to find an increasing trend. Therefore, we tried to fit the data with multiple power-law functions on restricted ranges of the distance (0.01-0.1pc, 0.1-10pc, and 3-100pc). We found that the power index of the best fit function ranged from 0.06 to 0.8, as shown in Figure 2. The multiple power-law functions indeed reveal the slow increasing trends of the brightness temperature in the regions of 0.01-0.1 pc and 3-100 pc, yielding power indices of 0.06 and 0.11, respectively. Therefore we concluded that the brightness temperature increases with different slopes (or power indices) in different regions for our data. Here caution should be taken for the fit results on the 0.01-0.1 pc regions, since there are only three data points (although those are all data we have for the region).

This result stimulated us to developing a single function suitable to model the overall evolution of the brightness temperatures along the jet. One of the best empirical models which we found has the

TABLE 1
STATISTICS OF BRIGHTNESS TEMPERATURE

ν (GHz) (1)	$T_{b,\text{med}}$ (K) (2)	$T_{b,\text{mean}}$ (K) (3)	σ_{T_b} (K) (4)	N (5)
2.3	4.5e+11	8.0e+11	9.2e+11	104
8.6	5.2e+11	8.5e+11	9.3e+11	104
15.4	4.5e+11	8.9e+11	1.1e+12	106
86.2	8.1e+10	1.3e+11	1.2e+11	44

NOTE.—Column designation: (1) - observing frequency; (2)-(3) - median and mean brightness temperatures; (4) - standard deviation of brightness temperature; (5) - number of brightness temperature used.

following form:

$$T_b = T_0 + (T_m - T_0)\{1 - (r \text{ cschr})^a\}, \quad (10)$$

where T_0 , T_m are the minimum (or initial) and maximum brightness temperatures in K, respectively, and r is the distance of the VLBI core components from the central engine in pc. This model assumes that T_0 is the brightness temperature near the jet base and T_m that in the downstream of the jet. We used $T_0 = 2.0 \times 10^{10}$ K which is corresponding to the mean of the observed brightness temperatures at $r = 0.02\text{--}0.1$ pc in Figure 2. The best fitting was obtained for $T_m = (9.2 \pm 0.7) \times 10^{11}$ K and $a = 0.9 \pm 0.3$, as shown in Figure 2. This implies that the brightness temperatures on sub-parsec scales are close to or even below the equipartition temperature of 5×10^{10} K (indicating that the jets may be magnetically dominated) and start to increase on (sub-)parsec regions, reaching the inverse Compton limit of $\sim 10^{12}$ K on parsec scales. Based on this best fitting model, we now can discuss specific jet parameters, like the the Doppler-factor and Lorentz factor. This is done in the next two sections.

4.2. Doppler factor

One of the possible and very simple ways to understand the variation of the brightness temperatures as a function of the distance is to assume that all of the observed variation in brightness temperatures is caused by a variation of the Doppler factor. Since the compact radio jets are highly relativistic, their synchrotron emission is Doppler boosted and the boosting effect is parametrized by the Doppler

factor. The Doppler factor is related to the physical properties of the relativistic jets such as the Lorentz factor γ_j , the intrinsic brightness temperature T_0 , and the jet viewing angle θ_j :

$$\delta = \frac{1}{\gamma_j(1 - \beta \cos\theta_j)}, \quad (11)$$

$$T_b = T_0 \delta, \quad (12)$$

where $\beta = (1 - \gamma_j^{-2})^{1/2}$ is the speed of the jet in the rest frame of the source in units of c .

In order to derive the evolution of the Doppler factor as a function of the distance r , equation (12) can be rewritten as

$$T_b = T_0 \left(\frac{\delta(r)}{\delta_0} \right), \quad (13)$$

where δ_0 is the Doppler factor at $r = r_{\text{min}}$. From equations (10) and (12), the Doppler factor $\delta(r)$ can be derived as

$$\delta(r) = \delta_0 \left[1 + \left(\frac{T_m}{T_0} - 1 \right) \{1 - (r \text{ cschr})^a\} \right], \quad (14)$$

where we assume that the minimum (or initial) brightness temperature in the model (equation (10)) is equal to the intrinsic brightness temperature. With this assumption, the inferred Doppler factor increases from $\delta_0 = 1$ to $\delta_m \sim 46$ in a similar way as the brightness temperature does, as shown in Figure 3 (top panel). The maximum Doppler factor δ_m constrains viewing angle θ_j in deducing the Lorentz factor as a function of the distance from the central engine, as below.

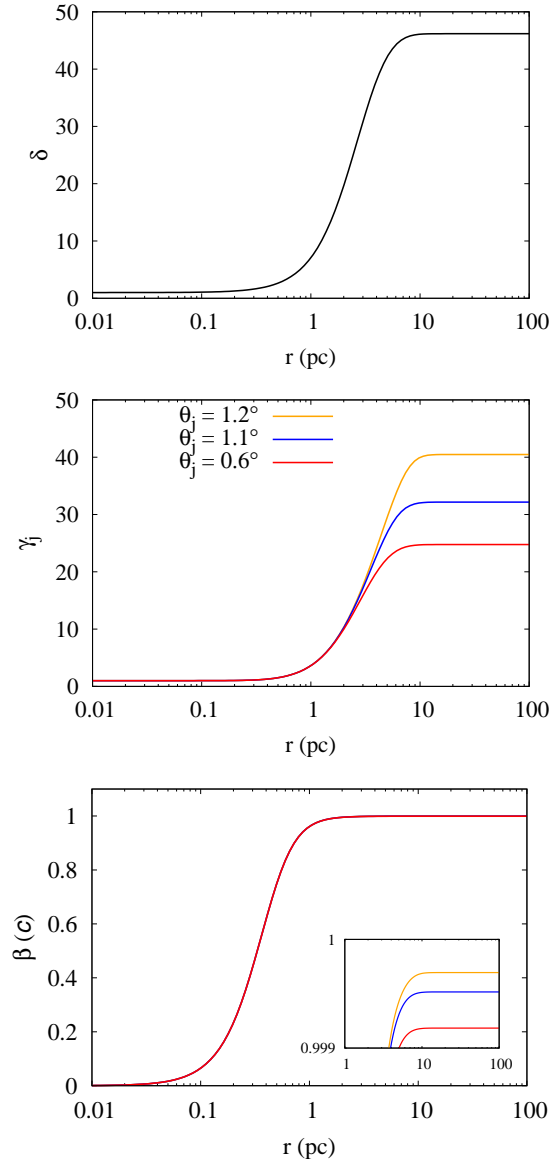


Fig. 3.— Plots of Doppler factor (top panel), Lorentz factor (middle), and the jet speed (bottom), with a zoom-in inset, as a function of the absolute position of the VLBI core components. The colored lines are for the jet viewing angles of $\theta_j = 1.2^\circ$ (orange), 1.1° (blue), and 0.6° (red). The initial Doppler factor is $\delta_0 = 1$.

4.3. Lorentz factor

One of the intrinsic properties of the relativistic jets, the Lorentz factor, can be deduced from

equation (11) which, can be rewritten as

$$\delta^2 \sin^2 \theta_j \gamma_j^2 - 2\delta \gamma_j + (1 + \delta^2 \cos^2 \theta_j) = 0. \quad (15)$$

For δ and θ_j satisfying the condition $\delta^2 \sin^2 \theta_j \leq 1$, a physically permitted solution of equation (15) is

$$\gamma_j = \frac{1 - \cos \theta_j \sqrt{1 - \delta^2 \sin^2 \theta_j}}{\delta \sin^2 \theta_j}. \quad (16)$$

By inserting equation (14) into equation (16), the dependence of the Lorentz factor on the distance from the central engine $\gamma_j(r)$ is deduced as shown in Figure 3 (middle panel), and according to the definition $\beta = (1 - \gamma_j^{-2})^{1/2}$ the evolution of the jet speed $\beta(r)$ is directly deduced as shown in Figure 3 (bottom panel). Here it should be noted that $\theta_j \leq 1/\delta_m$. Thus three examples of γ_j for $\theta_j = 0.6^\circ$, 1.1° , and 1.2° are shown. This picture matches very well with similar acceleration plots given for the magnetically driven, accelerating jet model (e.g., Vlahakis & Königl 2004; Lyubarsky 2009). Vlahakis & Königl (2004) argue that in the sub-parsec scale the mass flux is initially constant and then increasing, and in the outer region the mass flux becomes constant again. The Lorentz factor also shows a similar trend, being constant in the inner region and then increasing in the outer region. As the mass flux gets constant, the Lorentz factor also becomes constant in the outer region. We like to emphasize that such acceleration from sub-pc to pc-scales has been reported in a number of cases, such as NGC 6251 (Sudou et al. 2000) with moderately relativistic speeds ($0.13c \sim 0.42c$), Cygnus A (Bach et al. 2005; Boccardi et al. 2016) for apparent relativistic speeds ($0.2 \sim 0.5 h^{-1}c$), NGC 315 (Cotton et al. 1999) for parsec-scale jet acceleration ($0.75c \sim 0.95c$), M 87 (Asada et al. 2014) for jet acceleration from non-relativistic ($0.01c$) to relativistic ($0.97c$), and 3C 345 (Unwin et al. 1997; Lobanov & Zensus 1999) for highly relativistic speeds ($\gamma_\infty \approx 35$).

4.4. Opacity effects and core blending

The increase of core brightness temperature with decreasing frequency could also be at least partly due to an instrumental beam blending effect, with a larger observing beam size at lower frequencies. Therefore the fitted core region may

be diluted by jet emission, which comes from regions downstream of the $\tau = 1$ surface (see e.g., Hada et al. 2013). This blending effect will be more pronounced at the lower frequencies (2, 8, 15 GHz), because of the larger beam sizes.

The brightness temperature measurements at 2.3 GHz and 8.6 GHz are based on Pushkarev & Kovalev (2012). Using a part of the database, Kovalev et al. (2008) analyzed opacity effect (or core-shift effect) on the VLBI core measurements. They found that the median of the measured core shift between 2.3 GHz and 8.6 GHz is 0.44 mas with its maximum of 1.4 mas. They discussed the blending effect of the core and optically thin jet on the core shift measurements. They found that the blending shift of the core position has a distribution with its median value of 0.006 mas (see Figure 5 in Kovalev et al. 2008).

Based on this study we may be able to estimate the blending effect on the core flux measurement. Pushkarev & Kovalev (2012) found that the VLBI cores fitted with the circular Gaussian model had median values of their sizes of 1.04 mas and 0.28 mas at 2.3 GHz and 8.6 GHz, respectively. These results, in addition to the median value of core-shift of 0.44 mas, lead to a simple conical geometry of a jet as $d = 1.7r$ ($\frac{\delta d}{\delta r} = \frac{1.04-0.28}{0.44} = 1.7$), where d is the jet size and r is the distance from the jet base, assuming $r \propto \nu^{-1}$. Here, we may assume that the blending effect of 0.006 mas obtained from the 8.6 GHz data is similar to that for the 2.3 GHz data. Then the true position of the 2.3 GHz VLBI core, if it is observed with the beam of 8.6 GHz, would be shifted by 0.006 mas to the jet base, compared with the observed position of the 2.3 GHz VLBI core. According to the simple jet geometry, the true (or blending-free) size of the core may decrease by $\Delta d = 1.7\Delta r \sim 1.7 \times 0.006 \text{ mas} = 0.01 \text{ mas}$ which is 1% of its size of 1.04 mas obtained with the model fitting. If we assume that the $\tau = 1$ surface of the core has uniform brightness then the flux density of the true core may decrease by < 1%. This implies that the blending effect to the core flux density measurement may not be significant for the 2.3 GHz data with respect to the 8.6 GHz data.

We can also estimate the effect between the 8 GHz data and the 86 GHz data. Kovalev et al. (2008) also predicted that the expected core shift between 8.6 GHz and an optical wavelength of

6000 Angstrom would reach 0.12 mas which may be considered as the upper limit of the core shift between 8.6 GHz and 86 GHz (e.g., Hada et al. 2011). Lee et al. (2008) found that the 86 GHz VLBI cores fitted with the circular Gaussian model had median sizes of ~ 0.04 mas. These results again lead to a simple conical geometry of a jet as $d = 2r$ ($\frac{\delta d}{\delta r} = \frac{0.28-0.04}{0.12} = 2$). If we assume that the core blending effect to the core shift is proportional to the frequency difference (or resolution difference), then the blending effect would be as large as ~ 0.016 mas ($= \frac{86}{8.6} / \frac{8.6}{2.3} \times 0.006 \text{ mas}$) on the 8.6 GHz data with respect to the 86 GHz data. As a result, the true size of the 8.6 GHz core may decrease by $\Delta d = 2\Delta r \sim 2 \times 0.016 \text{ mas} = 0.032 \text{ mas}$ which is $\sim 13\%$ of the core size of 0.24 mas as obtained at 8.6 GHz with model fitting. Based on the constant brightness distribution of the $\tau = 1$ surface of the core at 8 GHz, the flux density S_ν of the true core may decrease by $\sim 24\%$. Then, we can estimate the fractional error (or blending effect) on the brightness temperature T_b using Gaussian error propagation as $\frac{\Delta T_b}{T_b} \approx \sqrt{(\frac{\Delta S_\nu}{S_\nu})^2 + 4(\frac{\Delta d}{d})^2} = 0.35$. The effect may be significant but is still small compared to the observed difference in the brightness temperature between 8.6 GHz and 86 GHz of a factor of 5-6 (see Table 1).

5. Conclusions

Due to the highly relativistic physical environments, the compact jets of extragalactic radio sources are Doppler boosted, making it impossible to directly measure their intrinsic properties: the intrinsic brightness temperature, the Lorentz factor, and the viewing angle. Under the equipartition condition between the magnetic field energy and particle energy density, the absolute distance of the VLBI core can be predicted, based on the facts that (a) the VLBI cores of the compact radio sources are optically thick at a given frequency, and (b) the distance of the core from the central engine is inversely proportional to the frequency. The multifrequency large VLBI surveys of the compact radio jets allowed the investigation of the source-frame brightness temperatures of the (sub-)parsec regions of the relativistic jets, yielding the following findings:

1. From the vicinity of the central engine to the outer region of the relativistic jets on (sub-)parsec scales, the brightness temperatures increase, implying that the energy of the radiating particles increases as they are driven out from the central engine in the (sub-)parsec scale regions.
2. The evolution of the brightness temperatures on the (sub-)parsec scales can be modeled, indicating that the brightness temperatures on sub-parsec scales are close to or even below the equipartition temperature of 5×10^{10} K and start to increase on (sub-)parsec regions, reaching the inverse Compton limit of $\sim 10^{12}$ K on parsec scales.
3. The evolution of the brightness temperatures directly reveals the dependence of the jet properties – the Doppler factor, the Lorentz factor, and the jet speed – on the distance from the central engine on (sub-)parsec scales, suggesting that the relativistic jets are magnetically driven to accelerate on the (sub-)parsec scale and travel at a constant speed on the parsec scales.

We would like to thank the anonymous referee for important comments and suggestions which have enormously improved the manuscript. This research has made use of data obtained with the Global Millimeter VLBI Array (GMVA), which consists of telescopes operated by the MPIfR, IRAM, Onsala, Metsahovi, Yebes and the VLBA. The data were correlated at the correlator of the MPIfR in Bonn, Germany. The VLBA is an instrument of the National Radio Astronomy Observatory, a facility of the National Science Foundation operated under cooperative agreement by Associated Universities, Inc

REFERENCES

Agudo, I., Bach, U., Krichbaum, T. P. et al. 2007, *A&A*, 476, L17

Asada, K., Nakamura, M., Doi, A., Nagai, H., & Inoue, M. 2014, *ApJ*, 781, L2

Attridge, J. M. 2001, *ApJ*, 553, L31

Bach, U., Kadler, M., Krichbaum, T. P. et al. 2005, *ASP Conf. Ser.* 340: *Future Directions in High Resolution Astronomy*, ed. J. Romney, & M. Reid

Boccardi, B., Krichbaum, T. P., Bach, U. et al. 2016, *A&A*, 585, 33

Baade, W. & Minkowski, R. 1954, *ApJ*, 119, 215

Beasley, A. J., Dhawan, V., Doeleman, S., & Phillips, R. B. 1997, in *Millimeter-VLBI Science Workshop*, ed. R. Barvainis & R. B. Phillips, 53–56

Blandford, R. D. & Königl, A. 1979, *ApJ*, 232, 34

Blandford, R. D. & Payne, D. G. 1982, *MNRAS*, 199, 883

Blandford, R. D. & Znajek, R. L. 1977, *MNRAS*, 179, 433

Blumenthal, G. R. & Gould, R. J. 1970, *Reviews of Modern Physics*, 42, 237

Bower, G. C., Backer, D. C., Wright, M., et al. 1997, *ApJ*, 484, 118

Bridle, A. H. & Perley, R. A. 1984, *ARA&A*, 22, 319

Cotton, W. D., Feretti, L., Giovannini, G., Lara, L. & Venturi, T. 1999, *ApJ*, 519, 108

Curtis, H. D. 1918, *Publications of Lick Observatory*, 13, 55

Doeleman, S. S. & Claussen, M. 1997, in *Millimeter-VLBI Science Workshop*, ed. R. Barvainis & R. B. Phillips, 37–38

Ferrari, A. 1998, *ARA&A*, 36, 539

Giochetti, G. B., Pérez-Torres, M. A., Chiaberge, M., et-al. 2008, *A&A*, 488, 905

Greiner, J., Klose, S., Reinsch, K., et al. 2003, *Nature*, 426, 157

Hada, K., Doi, A., Kino, M., Nagai, H., Hagiwara, Y. & Kawaguchi, N. 2011, *Nature*, 477, 185

Hada, K., Kino, M., Doi, et al. 2013, *ApJ*, 775, 70

Hada, K., Kino, M., Doi, A., et al. 2016, *ApJ*, 817, 131

TABLE 2
SYNCHROTRON LUMINOSITY

Name	z	$S_{86\text{ GHz}}$ (Jy)	$T_{b,86\text{ GHz}}$ (K)	$S_{15\text{ GHz}}$ (Jy)	$T_{b,15\text{ GHz}}$ (K)	$S_8\text{ GHz}$ (Jy)	$T_{b,8\text{ GHz}}$ (K)	$S_2\text{ GHz}$ (Jy)	$T_{b,2\text{ GHz}}$ (K)	L_{syn} (erg s $^{-1}$)	B_1 (G)
0003-066	0.347	1.760	2.6e+11	1.55	1.6e+11	1.53	1.5e+11	2.4e+45	1.20
0014+813	3.387	0.370	1.2e+11	0.54	5.2e+11	0.56	9.6e+11	6.1e+46	6.11
0016+731	1.781	0.510	4.5e+11	0.14	2.4e+10	0.68	3.5e+11	1.1e+46	2.59
0106+013	2.099	0.431	1.7e+11	1.870	1.6e+12	1.92	1.2e+12	3.7e+46	4.75
0112-017	1.365	0.255	4.6e+10	0.44	1.6e+11	0.80	1.7e+11	3.3e+45	1.42
0119+041	0.637	1.030	1.0e+11	0.53	6.9e+10	0.89	2.2e+11	4.5e+45	1.66
0119+115	0.57	0.910	1.5e+11	0.90	4.3e+11	1.27	6.0e+11	2.2e+45	1.15
0133+476	0.859	1.771	2.4e+11	2.675	5.0e+12	3.15	4.5e+12	1.38	7.4e+11	1.5e+46	3.03
0149+218	1.32	0.494	5.1e+10	1.040	7.2e+11	0.39	3.6e+11	1.2e+46	2.68
0201+113	3.639	0.590	4.7e+11	0.67	2.4e+11	0.84	2.2e+11	1.1e+47	8.20
0202+149	0.405	1.350	1.8e+11	1.84	5.2e+11	1.22	5.0e+11	9.0e+44	0.74
0202+319	1.466	0.614	7.9e+10	1.465	1.4e+12	1.37	2.0e+12	0.40	2.2e+11	1.9e+46	3.43
0234+285	1.206	0.986	2.4e+11	1.610	2.1e+11	3.48	1.8e+12	2.5e+46	3.93
0235+164	0.94	1.460	2.8e+12	1.30	8.7e+11	1.08	2.4e+12	1.9e+46	3.44
0238-084	0.005	0.267	2.0e+10	0.52	2.6e+10	0.61	2.4e+10	5.0e+40	0.01
0333+321	1.259	0.384	1.4e+11	1.050	2.7e+11	0.87	5.4e+11	0.89	2.7e+11	9.1e+45	2.36
0415+379	0.0491	1.104	4.1e+10	0.970	2.1e+10	0.45	1.4e+11	0.70	5.2e+10	2.5e+43	0.12
0430+052	0.033	1.107	5.4e+10	1.565	2.2e+11	0.84	8.6e+10	9.2e+42	0.08
0440-003	0.845	0.645	1.4e+11	0.45	2.2e+11	0.63	1.2e+11	5.2e+45	1.78
0521-365	0.05534	0.331	9.2e+09	1.750	5.9e+10	0.97	3.0e+11	0.91	9.3e+10	7.8e+42	0.07
0537-286	3.104	0.800	1.2e+12	0.91	6.2e+11	0.97	1.2e+12	1.1e+47	8.21
0552+398	2.363	0.480	2.2e+11	3.210	1.1e+12	3.53	1.3e+12	2.92	2.5e+12	7.6e+46	6.82
0602+673	1.97	0.930	2.8e+11	0.78	3.0e+11	0.84	1.7e+12	5.1e+46	5.60
0607-157	0.3226	0.965	2.9e+10	4.050	1.5e+12	3.19	1.4e+12	1.58	4.2e+11	9.4e+44	0.76
0615+820	0.71	0.285	1.4e+10	0.34	4.2e+10	0.52	6.9e+11	9.4e+44	0.76
0642+449	3.396	0.590	1.6e+11	2.490	2.8e+12	3.19	2.4e+12	0.84	3.4e+12	2.0e+47	11.04
0716+714	0.127	1.048	3.6e+11	0.85	2.1e+12	0.41	1.2e+12	1.7e+44	0.33
0727-115	1.591	2.870	3.7e+12	3.40	2.1e+12	2.50	3.1e+12	6.5e+46	6.30
0736+017	0.1894	0.832	1.0e+11	2.260	5.1e+11	0.35	9.3e+10	0.58	4.0e+10	2.4e+44	0.38
0738+313	0.631	0.447	3.6e+10	0.280	3.5e+11	0.74	1.3e+11	0.49	1.4e+11	2.4e+45	1.21
0742+103	2.624	0.750	9.4e+10	1.04	2.4e+11	1.32	1.1e+12	6.1e+46	6.12
0745+241	0.409	0.670	3.5e+11	0.35	2.0e+11	0.31	2.5e+11	2.3e+45	1.20
0748+126	0.889	0.679	1.6e+11	2.850	2.0e+12	1.55	2.0e+12	0.58	1.7e+11	7.2e+45	2.10
0804+499	1.436	0.140	6.2e+10	0.650	6.0e+11	0.48	5.2e+11	0.41	4.6e+11	5.6e+45	1.85
0814+425	0.530	0.311	2.3e+10	0.66	1.6e+12	0.78	3.9e+11	8.8e+44	0.73
0827+243	0.942	1.505	1.3e+12	0.79	8.6e+11	0.51	1.7e+11	4.0e+46	4.96
0850+581	1.3173	0.104	3.2e+10	0.060	7.2e+10	0.31	2.5e+11	0.40	3.8e+12	2.3e+45	1.19
0851+202	0.306	0.618	2.0e+11	1.260	1.4e+11	1.95	9.4e+11	1.60	3.7e+11	5.5e+44	0.58
0859+470	1.462	0.222	1.2e+11	0.510	2.6e+11	0.35	2.8e+10	7.1e+45	2.09
0917+449	2.180	0.865	1.8e+12	0.52	9.7e+11	0.25	2.2e+12	1.3e+47	9.08
0923+392	0.698	0.210	1.3e+10	0.33	1.9e+10	0.49	1.8e+11	6.1e+44	0.61
0945+408	1.249	0.363	5.0e+10	0.770	1.9e+11	0.76	3.3e+11	1.55	6.9e+11	8.7e+45	2.30
0955+476	1.873	1.680	5.2e+11	1.66	8.8e+11	1.09	2.9e+12	1.1e+47	8.17
1049+215	1.300	0.950	6.1e+11	0.33	4.0e+11	1.02	5.3e+11	1.2e+46	2.73
1055+018	0.888	1.370	4.4e+11	1.08	5.1e+11	1.24	3.6e+11	1.3e+46	2.80
1101+384	0.0308	0.292	2.1e+10	0.450	1.2e+11	0.29	3.1e+11	2.1e+42	0.04
1116+128	2.118	0.470	3.4e+11	0.71	3.9e+11	0.72	2.8e+11	2.5e+46	3.94
1124-186	1.048	1.240	3.5e+12	0.82	5.2e+11	0.92	4.2e+11	1.9e+46	3.44
1128+385	1.733	0.504	8.1e+10	0.570	5.0e+11	0.76	2.0e+12	2.3e+46	3.73
1145-071	1.342	0.640	1.4e+11	0.68	2.7e+11	0.43	3.8e+11	1.2e+46	2.74

TABLE 1
SYNCHROTRON LUMINOSITY (CONTINUED)

Name	z	$S_{86\text{ GHz}}$ (Jy)	$T_{b,86\text{ GHz}}$ (K)	$S_{15\text{ GHz}}$ (Jy)	$T_{b,15\text{ GHz}}$ (K)	$S_{8\text{ GHz}}$ (Jy)	$T_{b,8\text{ GHz}}$ (K)	$S_{2\text{ GHz}}$ (Jy)	$T_{b,2\text{ GHz}}$ (K)	L_{syn} (erg s $^{-1}$)	B_1 (G)
1150+812	1.25	1.055	5.8e+11	0.68	1.2e+12	0.41	5.0e+11	4.4e+46	5.21
1156+295	0.725	1.629	2.6e+11	0.910	5.7e+10	2.42	5.0e+12	1.22	3.5e+11	1.2e+46	2.71
1219+285	0.103	0.186	1.6e+10	0.280	8.5e+10	0.16	4.5e+10	0.18	3.7e+10	1.6e+43	0.10
1228+126	0.00436	1.046	1.8e+10	1.005	7.6e+10	1.29	5.9e+10	1.42	9.7e+10	1.6e+41	0.01
1244-255	0.638	1.220	8.0e+11	0.72	3.3e+11	0.81	3.3e+11	7.3e+45	2.11
1308+326	0.997	0.640	1.8e+11	1.130	2.3e+11	1.14	4.2e+11	7.7e+45	2.17
1324+224	1.40	0.530	2.1e+11	0.62	3.3e+11	0.70	1.6e+12	1.1e+46	2.59
1334-127	0.539	4.930	2.0e+12	4.07	9.1e+11	2.12	4.4e+11	3.7e+46	4.77
1404+286	0.077	0.850	4.7e+10	1.20	1.0e+11	1.56	9.5e+10	2.5e+43	0.12
1424+366	1.091	0.280	1.8e+10	0.12	5.3e+10	0.39	4.6e+11	2.1e+45	1.14
1508-055	1.191	0.503	4.6e+10	0.520	3.8e+11	0.41	2.7e+11	8.5e+45	2.28
1511-100	1.513	0.550	1.0e+11	0.590	2.8e+11	0.40	1.2e+11	0.60	3.9e+11	1.8e+46	3.27
1548+056	1.417	2.325	3.3e+11	2.13	5.9e+11	2.64	2.1e+12	5.1e+46	5.58
1555+001	1.772	0.680	1.3e+11	0.70	5.0e+11	0.56	7.2e+11	2.6e+46	4.02
1606+106	1.232	1.450	7.8e+11	2.46	2.0e+12	1.90	1.3e+12	9.7e+45	2.43
1611+343	1.401	2.745	1.8e+12	2.33	1.7e+12	2.10	6.2e+11	8.2e+46	7.08
1622-253	0.786	1.440	1.2e+12	1.58	1.4e+12	0.78	4.5e+11	7.5e+45	2.15
1624+416	2.55	0.260	2.1e+11	0.38	6.8e+11	0.57	1.7e+11	1.8e+46	3.35
1633+382	1.807	0.870	5.1e+11	0.73	3.6e+11	0.95	6.5e+11	3.3e+46	4.50
1637+574	0.751	1.145	3.2e+11	1.740	8.5e+11	1.07	4.9e+11	0.81	3.4e+11	7.0e+45	2.07
1638+398	1.666	1.135	8.6e+11	0.57	2.2e+11	0.82	6.4e+11	4.7e+46	5.36
1655+077	0.621	0.462	1.0e+11	1.745	2.0e+11	0.78	9.1e+10	0.58	9.5e+10	2.0e+45	1.11
1656+477	1.622	0.680	1.1e+12	0.60	8.3e+10	1.09	4.7e+11	1.6e+46	3.09
1730-130	0.902	6.875	5.7e+12	1.91	2.7e+12	2.53	3.9e+11	1.3e+47	9.00
1739+522	1.379	0.847	3.9e+11	0.730	3.8e+12	0.52	4.2e+12	0.43	2.9e+11	1.9e+46	3.43
1741-038	1.057	2.404	1.9e+11	4.695	2.7e+12	3.96	5.2e+11	3.01	9.7e+11	3.4e+46	4.54
1749+096	0.322	2.375	6.1e+11	3.715	2.2e+12	2.58	2.4e+12	1.70	3.2e+12	2.2e+45	1.16
1758+388	2.092	1.270	6.9e+11	0.89	6.5e+11	0.30	5.2e+11	2.3e+47	11.74
1803+784	0.6797	0.785	8.0e+10	1.555	6.3e+11	1.52	1.7e+12	1.27	9.6e+11	4.0e+45	1.56
1807+698	0.051	0.640	1.0e+11	0.36	3.9e+11	0.49	5.1e+11	1.7e+43	0.10
1821+107	1.364	0.270	7.1e+10	0.39	2.0e+11	0.73	4.5e+11	3.5e+45	1.47
1823+568	0.664	0.485	1.4e+11	0.850	2.1e+11	0.75	8.7e+11	0.40	9.9e+11	2.3e+45	1.17
1849+670	0.657	1.610	1.8e+12	0.91	2.9e+12	0.33	6.4e+11	4.0e+46	4.95
1908-201	1.119	2.600	5.3e+11	0.99	3.4e+11	1.17	1.7e+11	6.7e+46	6.42
1921-293	0.3526	2.069	3.9e+10	7.720	4.5e+11	6.66	5.2e+11	6.16	1.6e+11	2.5e+45	1.24
1937-101	3.787	0.215	1.1e+11	0.35	1.4e+11	0.35	9.4e+11	4.7e+46	5.34
1954+513	1.223	0.279	1.8e+11	0.620	4.5e+11	0.37	1.0e+12	0.33	5.3e+12	5.7e+45	1.86
1954-388	0.630	2.320	5.0e+11	3.42	1.5e+12	1.69	7.5e+11	3.6e+45	1.48
1958-179	0.652	1.775	1.1e+12	1.73	1.1e+12	1.47	9.0e+11	9.8e+45	2.45
2029+121	1.215	0.760	3.9e+11	0.66	5.2e+11	0.36	8.3e+11	2.6e+46	4.02
2113+293	1.514	0.615	3.8e+11	0.45	1.0e+12	0.63	1.7e+12	1.6e+46	3.09
2121+053	1.941	0.414	8.7e+10	2.150	2.6e+12	2.09	1.6e+12	4.0e+46	4.97
2126-158	3.28	1.110	8.6e+11	0.75	7.5e+11	0.77	6.8e+11	2.1e+47	11.40
2128-123	0.501	0.500	5.8e+10	2.92	2.3e+11	1.65	1.1e+11	2.8e+44	0.41
2131-021	1.285	1.120	2.4e+11	1.20	2.2e+11	1.29	1.0e+12	2.1e+46	3.55
2136+141	2.427	1.260	8.2e+11	1.81	1.2e+12	1.00	1.0e+12	5.9e+46	6.00
2145+067	0.999	5.255	3.4e+12	4.21	1.8e+12	2.66	1.0e+12	1.1e+47	8.32
2200+420	0.0686	1.870	4.3e+11	1.22	1.0e+12	1.42	2.0e+11	9.8e+43	0.24
2201+315	0.2947	0.817	5.0e+10	2.070	3.2e+11	0.78	1.4e+12	0.86	1.9e+11	6.2e+44	0.62
2209+236	1.125	1.040	5.3e+11	1.42	1.4e+12	0.74	1.9e+12	7.6e+45	2.16

TABLE 1
SYNCHROTRON LUMINOSITY (CONTINUED)

Name	z	$S_{86 \text{ GHz}}$ (Jy)	$T_{b,86 \text{ GHz}}$ (K)	$S_{15 \text{ GHz}}$ (Jy)	$T_{b,15 \text{ GHz}}$ (K)	$S_8 \text{ GHz}$ (Jy)	$T_{b,8 \text{ GHz}}$ (K)	$S_2 \text{ GHz}$ (Jy)	$T_{b,2 \text{ GHz}}$ (K)	L_{syn} (erg s^{-1})	B_1 (G)
2216–038	0.901	2.025	5.3e+11	1.43	8.7e+11	0.37	2.6e+11	1.1e+47	8.15
2223–052	1.404	0.642	7.3e+10	3.740	1.2e+12	3.49	1.3e+12	2.39	2.6e+12	2.7e+46	4.04
2227–088	1.562	2.030	2.0e+12	0.43	6.4e+10	0.77	2.7e+11	1.1e+47	8.13
2230+114	1.037	2.680	2.1e+12	1.74	1.0e+12	2.34	3.0e+11	3.5e+46	4.64
2234+282	0.79	0.405	4.4e+10	0.210	1.5e+10	1.22	3.5e+11	1.80	1.4e+12	2.7e+45	1.28
2243–123	0.630	1.920	5.1e+11	1.11	1.2e+11	1.38	4.2e+11	1.0e+46	2.49
2255–282	0.927	5.650	4.9e+12	5.99	1.0e+12	0.89	1.8e+11	4.6e+46	5.33
2329–162	1.153	0.610	4.7e+10	0.93	1.4e+11	0.91	1.2e+11	4.0e+45	1.57
2345–167	0.576	1.215	2.5e+11	1.52	4.2e+11	0.92	2.2e+11	2.2e+45	1.17

- Harris, D. E. & Krawczynski, H. 2006, *ARA&A*, 44, 463
- Heinz, S. & Begelman, M. C. 2004, *ApJ*, 535, 104
- Homan, D. C., Kovalev, Y. Y., Lister, M. L., et al. 2006, *ApJ*, 642, L115
- Kellermann, K. I. & Pauliny-Toth, I. I. K. 1981, *ARA&A*, 19, 373
- Königl, A. 1981, *ApJ*, 243, 700
- Kovalev, Y. Y., Kellermann, K. I., Lister, M. L., et al. 2005, *AJ*, 130, 2473
- Kovalev, Y. Y., Lobanov, A. P., Pushkarev, A. B., & Zensus, J. A. 2008, *A&A*, 483, 759
- Koyama, S., Kino, M., Giroletti, M., et al. 2016, *A&A*, 586, 113
- Kulkarni, S. R., Djorgovski, S. G., Odewahn, S. C., et al. 1999, *Nature*, 398, 389
- Krichbaum, T. P., Britzen, S., Standke, K. J., et al. 1995, *Proceedings of the National Academy of Science*, 92, 11377
- Krichbaum, T. P., Witzel, A., & Zensus, J. A. 1999, in *2nd Millimeter-VLBI Science Workshop*, ed. A. Greve & T. Krichbaum, 5–8
- Krichbaum, T. P., Graham, D. A., Bremer, M. et al. 2006, *Journal of Physics Conference Series*, 54, 328
- Lee, S.-S., Lobanov, A. P., Krichbaum, T. P., et al. 2008, *AJ*, 136, 159
- Lee, S. S. 2013, *JKAS*, 46, 243
- Lee, S. S. 2014, *JKAS*, 47, 303
- Lee, S. S., Kang, S., Byun, D. Y., et al. 2015, *ApJ*, 808, L26
- Lister, M. L., Cohen, M. H., Homan, D. C., et al. 2009, *AJ*, 138, 1874
- Lobanov, A. P. 1998, *A&A*, 330, 79
- Lobanov, A. P. 2005, arXiv astro-ph/0503225
- Lobanov, A. P. & Zensus, J. A. 1999, *ApJ*, 521, 509
- Lobanov, A. P., Krichbaum, T. P., Graham, D. A., et al. 2000, *A&A*, 364, 391
- Lonsdale, C. J., Doeleman, S. S., & Phillips, R. B. 1998, *AJ*, 116, 8
- Lovelace, R. V. E. 1976, *Nature*, 262, 649
- Lovelace, R. V. E. & Romanova, M. M. 2003, *ApJ*, 596, L159
- Lyubarsky, Y. 2009, *ApJ*, 698, 1570
- Martí-Vidal, I., Krichbaum, T. P., Marscher, A., et al. 2012, *A&A*, 542, 107
- McKinney, J. C. & Blandford, R. D. 2009 *MNRAS*, 394, 126
- Mirabel, I. F. & Rodriguez, L. F. 1994 *Nature*, 371, 46
- Mirabel, I. F. & Rodriguez, L. F. 1998 *Nature*, 392, 673
- Molina, S. N., Agudo, I., Gómez, J. L., Krichbaum, T. P., Martí-Vidal, I., & Roy, A.L. 2014 *A&A*, 566, 2

- Nokhrina, E. E., Beskin, V. S., Kovalev, Y. Y., & Zheltoukhov, A. A. 2015 MNRAS, 447, 2726
- Pagels, A., Krichbaum, T. P., Graham, D. A., et al. 2004, in European VLBI Network on New Developments in VLBI Science and Technology, ed. R. Bachiller, F. Colomer, J.-F. Desmurs, & P. de Vicente, 7–10
- Pushkarev, A. B. & Kovalev, Y. Y. 2012, A&A, 544, 34
- Rani, B., Krichbaum, T. P., Marscher, A. P., et al. 2015, A&A, 578, 123
- Rantakyrö, F. T., Baath, L. B., Backer, D. C., et al. 1998, A&AS, 131, 451
- Rees, M. J. 1966, Nature, 211, 468
- Rybicki, G. B. & Lightman, A. P. 1979, Radiative processes in astrophysics (New York, Wiley-Interscience)
- Sikora, M. & Madejski, G. 2000, ApJ, 534, 109
- Sudou, H., Taniguchi, Y., Ohyama, Y., et al. 2000, PASJ, 52, 989
- Toma, K. & Takahara, F. 2014, MNRAS, 442, 2855
- Unwin, S. C., Wehrle, A. E., Lobanov, A. P., et al. 1997, ApJ, 480, 596
- Vlahakis, N. & Königl, A. 2004, ApJ, 605, 656
- Walker, R. C. and Benson, J. M. and Unwin, S. C., et al. 2001, ApJ, 556, 756
- Whitney, A. R., Shapiro, I. I., Rogers, A. E. E., et al. 1971, Science, 173, 225
- Zensus, J. A. 1997, ARA&A, 35, 607

This 2-column preprint was prepared with the AAS L^AT_EX macros v5.2.